Second-harmonic generation from periodic arrays of arbitrary shape plasmonic nanostructures: a surface integral approach

Jérémy Butet,[1,*] Benjamin Gallinet,[2] Krishnan Thyagarajan,[1] and Olivier J. F. Martin[1]

[1]*Nanophotonics and Metrology Laboratory (NAM), Swiss Federal Institute of Technology Lausanne (EPFL), 1015 Lausanne, Switzerland*
[2]*Centre Suisse d'Electronique et de Microtechnique (CSEM), 4132 Muttenz, Switzerland*
Corresponding author: jeremy.butet@epfl.ch

A surface integral formulation for the second-harmonic generation (SHG) from periodic metallic–dielectric nanostructures is described. This method requires the discretization of the scatterers' surface in the unit cell only. All the physical quantities involved in this problem are derived in the unit cell by applying specific periodic boundary conditions both at the fundamental and the second-harmonic (SH) frequencies. Both the fundamental and the SH electric fields are computed using the method of moments and periodic Green's function evaluated with the Ewald's method. The accuracy of the method is carefully assessed using two specific cases, namely the surface plasmon enhancement of SHG from a gold film and the SHG from L-shaped nanoparticle arrays. These two examples emphasize the accuracy and versatility of the proposed method, which can be applied to a broad range of periodic metallic structures, including plasmonic arrays on arbitrary substrates and metamaterials.   © 2013 Optical Society of America

OCIS codes: (190.2620) Harmonic generation and mixing; (240.4350) Nonlinear optics at surfaces; (250.5403) Plasmonics.

http://dx.doi.org/10.1364/JOSAB.30.002970

1. INTRODUCTION

Nonlinear plasmonics, the study of nonlinear optical processes in metals, is a growing field opening new perspectives for the control of light down to the nanoscale and optical signal modulation [1]. This interest is mainly triggered by the strong electric field enhancement caused by surface plasmon resonances occurring in metallic nanostructures, which dramatically increases the efficiency of nonlinear optical processes [1]. Among the different nonlinear parametric optical phenomena, optical second-harmonic generation (SHG), the optical process whereby two photons at the fundamental wavelength are converted into one photon at the second-harmonic (SH) wavelength, is probably the most studied in plasmonic nanostructures [1–36]. Experimental data report the SHG from assemblies [3,4] and single spherical metallic nanoparticles [5], noncentrosymmetric nanocups [6], optical nanoantennas [7–9], split-ring resonators [10], plasmonic metamolecules [11], metallic nanotips [12,13], periodic arrays of nanodots [14], L-shaped [15,16] and G-shaped [17,18] gold nanoparticle periodic arrays, as well as aperiodic arrays of nanoparticles [14,19]. It was recently demonstrated that SHG is a very efficient tool for the optical characterization of metallic nanoobjects [20,21] and that it is also sensitive to the nanoparticle's spatial distribution [22]. Furthermore, the intrinsic properties of SHG can increase the performances of plasmonic sensors [23]. SHG from centrosymmetric media is forbidden in the electric dipole approximation, which limits the total SHG signal. However, the centrosymmetry is broken at the interface between nanostructures and their embedding

media, making SHG possible. The role played by bulk contributions induced by field gradients in the nanostructures has also been discussed [24,25].

A good understanding of the SHG from metallic nanostructures requires the development of appropriate models and numerical simulation tools. While the SHG from spherical homogeneous nanospheres and nanoshells can be handled with nonlinear Mie theories [26–29], this is not the case for more complex geometries. As a consequence, several numerical schemes have been developed, such as the finite elements method [30], boundary elements method (BEM) [31], hydrodynamic models [32,35], finite-difference time-domain (FDTD) [36,37], volume integral equations (VIE) [38], and the surface integrals equations (SIE) method [21,39]. Among all these methods, SIE and BEM are particularly appropriated for the computation of the surface SHG from nanoparticles, since they only require the discretization of the scatterer surface. Furthermore, it was shown that the computation of the electromagnetic near-field, which is a key for precise SHG computation, is more accurate using SIE than VIE [40,41].

While several authors have reported the computation of SHG from single nanostructures, very little has been published on the numerical evaluation of the SHG in periodic arrays of plasmonic nanostructures. Although a few numerical methods, such as coupled-wave analysis [42], Fourier modal method [43], or a combination of analytic parametrizations of SHG and numerical FDTD evaluations [44], have been developed for the computation of SHG from periodic metallic

structures, versatile and general methods that can handle arbitrary structures are also required. It was recently demonstrated that the linear optical response of periodic structures can be computed with the SIE method using a periodic Green's function [45,46]. The main difference between the SIE computation of light scattering by individual and periodic scatterers is the utilizations of a periodic Green's function for the latter. The computation of this periodic Green's function is quite time consuming, but can be performed efficiently using Ewald's method [45–47].

In this paper, a surface integral formulation for SHG from periodic plasmonic nanostructures is developed. The fundamental electric field is first computed using a numerical scheme previously established for the investigation of the linear response of such a periodic system [45,46]. The nonlinear polarization, i.e., the SH source, is then evaluated at the different metallic interfaces in the system. A surface integral formulation for SHG is then applied by considering the periodicity of the SH electromagnetic field. Both the fundamental and SH surface currents are expanded on Rao–Wilton–Glisson (RWG) functions [48] and the Poggio–Miller–Chang–Harrington–Wu–Tsai (PMCHWT) formulation is applied to ensure accurate solutions even at resonant conditions [49]. The evaluation of the periodic Green's functions is performed by the Ewald's method [47]. The accuracy of the proposed method is finally assessed in two specific cases. First, the surface plasmon enhancement of SHG from a gold film is considered, showing that the computed spectral response is in perfect agreement with phenomenological predictions. As a second example, the SHG from L-shaped nanoparticle arrays is considered demonstrating that the computed SH fields fulfill the required symmetry properties imposed by the sample geometry.

2. SURFACE INTEGRAL EQUATIONS FOR THE FUNDAMENTAL FIELD IN PERIODIC STRUCTURES

In this section, the optical properties of the periodic structures are evaluated at the fundamental frequency. We follow exactly the same procedure as in [45] for computing the fundamental field in the periodic structure and provide here only the main results. For SHG, the purpose is to first obtain the linear surface current densities which are required for the evaluation of the nonlinear sources.

A. Electric and Magnetic Field Integral Equations for Periodic Structures

We will focus on lattices in 2 dimensions, corresponding to the most experimentally relevant situation, but this approach can handle periodicity in 1, 2, and 3 dimensions [45]. A lattice vector $\mathbf{t}$ is a linear combination $\mathbf{t} = \sum_{i=1,2} c_i \mathbf{a}_i$ where c_i is an integer and $\mathbf{a}_i$ are the primitive lattice vectors. The unit cell of the lattice is called Ω. The unit cell contains N domains V_n^Ω $n = 1, \ldots N$ with dielectric permittivity ε_n and magnetic permeability μ_n. The irreducible representation of the translation group is associated to a Bloch wavevector $\mathbf{k}$ in the first Brillouin zone. The Bloch functions $\mathbf{U_k}$ satisfy the Floquet-periodic conditions

$$\mathbf{U_k}(\mathbf{r} - \mathbf{t}) = e^{i\mathbf{k}\cdot\mathbf{t}}\mathbf{U_k}(\mathbf{r}). \qquad (1)$$

The incident field and the surface current densities are projected onto this space. The corresponding projections are

denoted $\mathbf{E}_{n,\mathbf{k}}^{\text{inc}}$, $\mathbf{H}_{n,\mathbf{k}}^{\text{inc}}$, $\mathbf{J}_{n,\mathbf{k}}$, and $\mathbf{M}_{n,\mathbf{k}}$, respectively. The computation of the electric field integral equation (EFIE) and the magnetic field integral equation (MFIE) can then be restricted to boundary surfaces $\partial V_n^\Omega \equiv \partial V_n \cap \Omega$ in the unit cell Ω [45]

$$
\begin{aligned}
&\left(i\omega\mu_n \int_{\partial V_n^\Omega} \mathrm{d}S' \bar{\mathbf{G}}_{n,\mathbf{k}}(\mathbf{r},\mathbf{r}') \cdot \mathbf{J}_{n,\mathbf{k}}(\mathbf{r}') \right.\\
&\left. + \int_{\partial V_n^\Omega} \mathrm{d}S'[\nabla \times \bar{\mathbf{G}}_{n,\mathbf{k}}(\mathbf{r},\mathbf{r}')] \cdot \mathbf{M}_{n,\mathbf{k}}(\mathbf{r}') \right)_{\parallel}\\
&= (\mathbf{E}_{n,\mathbf{k}}^{\text{inc}}(\mathbf{r}))_{\parallel}, \qquad \mathbf{r} \in \partial V_n^\Omega \qquad (2)
\end{aligned}
$$

and

$$
\begin{aligned}
&\left(i\omega\varepsilon_n \int_{\partial V_n^\Omega} \mathrm{d}S' \bar{\mathbf{G}}_{n,\mathbf{k}}(\mathbf{r},\mathbf{r}') \cdot \mathbf{M}_{n,\mathbf{k}}(\mathbf{r}') \right.\\
&\left. - \int_{\partial V_n^\Omega} \mathrm{d}S'[\nabla \times \bar{\mathbf{G}}_{n,\mathbf{k}}(\mathbf{r},\mathbf{r}')] \cdot \mathbf{J}_{n,\mathbf{k}}(\mathbf{r}') \right)_{\parallel}\\
&= (\mathbf{H}_{n,\mathbf{k}}^{\text{inc}}(\mathbf{r}))_{\parallel}, \qquad \mathbf{r} \in \partial V_n^\Omega. \qquad (3)
\end{aligned}
$$

The subscript $\parallel$ denotes the tangential component of the fields. The fields

$$\mathbf{E}_{n,\mathbf{k}}^{\text{inc}}(\mathbf{r}') = i\omega\mu_n \int_{V_n^\Omega} \mathrm{d}V \bar{\mathbf{G}}_{n,\mathbf{k}}(\mathbf{r}',\mathbf{r}) \cdot \mathbf{j}(\mathbf{r}) \qquad (4)$$

and

$$\mathbf{H}_{n,\mathbf{k}}^{\text{inc}}(\mathbf{r}') = \int_{V_n^\Omega} \mathrm{d}V[\nabla \times \mathbf{j}(\mathbf{r})] \cdot \bar{\mathbf{G}}_{n,\mathbf{k}}(\mathbf{r},\mathbf{r}') \qquad (5)$$

are the incident electric and magnetic fields, respectively, generated by the electrical current density $\mathbf{j}(\mathbf{r})$ in the region V_n^Ω. The dyadic $\bar{\mathbf{G}}_{n,\mathbf{k}}(\mathbf{r},\mathbf{r}')$ is the periodic Green's function

$$\bar{\mathbf{G}}_{n,\mathbf{k}}(\mathbf{r},\mathbf{r}') = \sum_{\mathbf{t}} e^{i\mathbf{k}\cdot\mathbf{t}} \bar{\mathbf{G}}_n(\mathbf{r}-\mathbf{t},\mathbf{r}'), \qquad (6)$$

satisfying the relation $\bar{\mathbf{G}}_{n,\mathbf{k}}(\mathbf{r}-\mathbf{t},\mathbf{r}') = e^{-i\mathbf{k}\cdot\mathbf{t}}\bar{\mathbf{G}}_{n,\mathbf{k}}(\mathbf{r},\mathbf{r}')$. The periodic Green's functions are evaluated using the Ewald's method [45,47]. For simplicity, the label $\mathbf{k}$ is omitted in the following.

B. Solution by the Method of Moments
In this section, the method of moments for solving the EFIE (2) and MFIE (3) is introduced [50]. The electric and magnetic surface densities are expanded on the RWG basis functions $\mathbf{f}_i^n$ building a triangular mesh approximating the boundary surface ∂V_n^Ω [47]

$$\mathbf{J}_n = \sum_i \alpha_i \mathbf{f}_i^n, \qquad (7)$$

$$\mathbf{M}_n = \sum_i \beta_i \mathbf{f}_i^n, \qquad (8)$$

where the summations occur on all the mesh edges. The conservation of the currents on the boundary between the domains n and n' implies that $\mathbf{f}_i^n = -\mathbf{f}_i^{n'}$. Applying the Galerkin's method and defining the sets $\{\alpha\}$ and $\{\beta\}$ as the sets of the surface current expansion coefficients, the EFIE and MFIE

are combined following the PMCHWT formulation in order to ensure stable and accurate results even under resonant conditions [46]

$$
\begin{bmatrix}
\sum_n i\omega\mu_n D^n & \sum_n K^n \\
\sum_n K^n & -\sum_n i\omega\varepsilon_n D^n
\end{bmatrix}
\cdot
\begin{bmatrix}
\{\alpha\} \\
\{\beta\}
\end{bmatrix}
= \sum_n
\begin{bmatrix}
\mathbf{q}^{(E),n} \\
\mathbf{q}^{(H),n}
\end{bmatrix}, \quad (9)
$$

where the summations are performed over all the domains n and where the following submatrices are introduced:

$$
D_{i,j}^n = \int_{\partial V_n^\Omega} \mathrm{d}S \mathbf{f}_i^n(\mathbf{r}) \cdot \int_{\partial V_n^\Omega} \mathrm{d}S' \bar{\mathbf{G}}_n(\mathbf{r},\mathbf{r}') \cdot \mathbf{f}_j^n(\mathbf{r}'), \qquad (10)
$$

$$
K_{i,j}^n = \int_{\partial V_n^\Omega} \mathrm{d}S \mathbf{f}_i^n(\mathbf{r}) \cdot \int_{\partial V_n^\Omega} \mathrm{d}S' [\nabla' \times \bar{\mathbf{G}}_n(\mathbf{r},\mathbf{r}')] \cdot \mathbf{f}_j^n(\mathbf{r}'), \qquad (11)
$$

$$
q_i^{(E),n} = \int_{\partial V_n^\Omega} \mathrm{d}S \mathbf{f}_i^n(\mathbf{r}) \cdot \mathbf{E}_n^{\mathrm{inc}}(\mathbf{r}), \qquad (12)
$$

$$
q_i^{(H),n} = \int_{\partial V_n^\Omega} \mathrm{d}S \mathbf{f}_i^n(\mathbf{r}) \cdot \mathbf{H}_n^{\mathrm{inc}}(\mathbf{r}). \qquad (13)
$$

The integrals (10)–(13) can be computed numerically using Gaussian quadrature [51]. Unfortunately, the integrals in Eqs. (10) and (11) relative to the same triangle element diverge. Furthermore, inaccurate results can also be obtained for matrix elements associated with neighboring triangles. A regularization scheme, including a singularity subtraction [52], is applied (see the appendix of [45]). The expansion coefficients are obtained solving the set of linear equations with LU decomposition. Finally, the electric and magnetic fields scattered by the periodic nanostructures are given by

$$
\mathbf{E}_n^{\mathrm{scat}}(\mathbf{r}) = \sum_i -i\omega\mu_n \int_{\partial V_n^\Omega} \mathrm{d}S' \bar{\mathbf{G}}_n(\mathbf{r}',\mathbf{r}) \cdot \alpha_i \mathbf{f}_i^n(\mathbf{r}')
$$
$$
- \int_{\partial V_n^\Omega} \mathrm{d}S' [\nabla' \times \bar{\mathbf{G}}_n(\mathbf{r}',\mathbf{r})] \cdot \beta_i \mathbf{f}_i^n(\mathbf{r}'), \qquad (14)
$$

$$
\mathbf{H}_n^{\mathrm{scat}}(\mathbf{r}) = \sum_i -i\omega\varepsilon_n \int_{\partial V_n^\Omega} \mathrm{d}S' \bar{\mathbf{G}}_n(\mathbf{r}',\mathbf{r}) \cdot \beta_i \mathbf{f}_i^n(\mathbf{r}')
$$
$$
+ \int_{\partial V_n^\Omega} \mathrm{d}S' [\nabla' \times \bar{\mathbf{G}}_n(\mathbf{r}',\mathbf{r})] \cdot \alpha_i \mathbf{f}_i^n(\mathbf{r}'). \qquad (15)
$$

In the following section, we use the currents from the linear calculation as sources to develop a surface integral equation formulation for the SHG from periodic structures.

3. SURFACE INTEGRAL EQUATIONS FOR THE SECOND-HARMONIC GENERATION FROM PERIODIC STRUCTURES

A surface integral formulation for the SHG from isolated scatterers has already been developed by Mäkitalo *et al.* [31]. Using a similar approach, we develop in this section a surface integral formulation for the SHG from periodic structures

composed of dielectric and metallic domains. The source of SHG is the nonlinear polarization oscillating at the SH frequency. It is well known that SHG is forbidden in the bulk of centrosymmetric media in the dipolar approximation. Even if nonlocal bulk sources could also contribute to the SHG from metal, only local surface contributions will be considered in the following since these sources are known to be the dominant ones [24,25]. Note that the nonlocal bulk sources for SHG can be included following Forestiere *et al.* [39]. With this assumption, the nonlinear polarization is given by

$$
\mathbf{P}(\mathbf{r}^+) = \chi^{(2)} : \mathbf{E}(\mathbf{r}^-)\mathbf{E}(\mathbf{r}^-). \qquad (16)
$$

The + and – subscripts denote that the nonlinear polarization sheet is located just above the metal and the fundamental electric field is estimated just below the interface [53,54]. Due to the symmetry of the interface, only the $\chi_{\perp\perp\perp}^{(2)}$, $\chi_{\perp\|\|}^{(2)}$ and $\chi_{\|\|\perp}^{(2)} = \chi_{\|\perp\|}^{(2)}$ components of the nonlinear susceptibility $\chi^{(2)}$ are nonvanishing, where $\perp$ denotes the component normal to the interface and $\|$ denotes the tangential component. Either experimental [24,25,55] or theoretical values [56,57] of the nonlinear susceptibility can be included in our model. The computation of the nonlinear polarization requires the evaluation of the fundamental electric field just below the metallic interface [53,54]. The corresponding electric field is related to the electric and magnetic surface current densities by [31]

$$
\mathbf{M}_m = -\mathbf{E}_m \times \hat{\mathbf{n}}_m, \qquad \nabla_\| \cdot \mathbf{J}_m = -i\omega\varepsilon_m \hat{\mathbf{n}}_m \cdot \mathbf{E}_m, \qquad (17)
$$

where m denotes the domain corresponding to the metallic part of the periodic structures in which the fundamental field is evaluated and $\hat{\mathbf{n}}_n$ is the outward normal vector on boundary ∂V_n. The fundamental electric field used for the computation of the nonlinear polarization satisfies the Floquet-periodic conditions (1). This relation induces the following constraint for the nonlinear polarization:

$$
\mathbf{P_K}(\mathbf{r}^+ - \mathbf{t}) = e^{i\mathbf{K}.\mathbf{t}}\mathbf{P_K}(\mathbf{r}^+), \qquad (18)
$$

where $\mathbf{K} = 2\mathbf{k}$ is the Bloch vector associated to the SH waves. The next step is the development of a surface integral formulation for the SH field. Following Mäkitalo *et al.* [31], we start from the boundary conditions for the SH field including the nonlinear polarization sheet standing at the interfaces between the domains m and d [58]

$$
(\Delta \mathbf{E}^{\mathrm{SH}})_\| = (\mathbf{E}_d^{\mathrm{SH}}(\mathbf{r}^+) - \mathbf{E}_m^{\mathrm{SH}}(\mathbf{r}^-))_\| = -\frac{1}{\varepsilon'}\nabla_\| P_\perp, \qquad (19)
$$

$$
(\Delta \mathbf{H}^{\mathrm{SH}})_\| = (\mathbf{H}_d^{\mathrm{SH}}(\mathbf{r}^+) - \mathbf{H}_m^{\mathrm{SH}}(\mathbf{r}^-))_\| = -2\omega\mathbf{P} \times \hat{\mathbf{n}}_m, \qquad (20)
$$

where ε' is the so-called selvedge region permittivity [50]. The indexes m and d denote the metallic and the dielectric side of the considered interface, respectively. As for the fundamental wave, the SH problem is solved using the method of moments and expanding the equivalent SH surface densities on the RWG functions [48]

$$
\mathbf{J}_m^{\mathrm{SH}} = \sum_i \alpha_i^{m,\mathrm{SH}} \mathbf{f}_i^m, \qquad (21)
$$

$$\mathbf{M}_m^{\mathrm{SH}} = \sum_i \beta_i^{m,\mathrm{SH}} \mathbf{f}_i^m, \tag{22}$$

for the surface currents flowing in the metal and

$$\mathbf{J}_d^{\mathrm{SH}} = \sum_i \gamma_i^{d,\mathrm{SH}} \mathbf{f}_i^d, \tag{23}$$

$$\mathbf{M}_d^{\mathrm{SH}} = \sum_i \delta_i^{d,\mathrm{SH}} \mathbf{f}_i^d, \tag{24}$$

for the surface currents flowing in the dielectric above the metal. Contrary to the case of the fundamental surface currents, the magnitudes of the SH surface currents standing at both sides of a given interface are different due to the nonlinear polarization existing at the interface. Nevertheless, the equality $\mathbf{J}_m^{\mathrm{SH}} = -\mathbf{J}_d^{\mathrm{SH}}$ stands if only the component $P_\perp$ is relevant, as is the case for SHG from metallic interfaces [24,25]. Therefore, and without loss of generality, only the component $P_\perp$ of the nonlinear source will be considered in the following. In this case, the equality $\alpha_i^{m,\mathrm{SH}} = \gamma_i^{d,\mathrm{SH}}$ stands and the corresponding expansion coefficient is noted α_i^{SH} in the following. Using Galerkin's test, the following linear system of equations is derived from the boundary conditions (19) and (20):

$$\begin{bmatrix} \sum_{m,d} i2\omega\mu_n D^{\mathrm{SH},n} & \sum_m K^{\mathrm{SH},n} & -\sum_d K^{\mathrm{SH},n'} \\ -\sum_{m,d} K^{\mathrm{SH},n} & \sum_m i2\omega\varepsilon_n D^{\mathrm{SH},n} & -\sum_d i2\omega\varepsilon_n D^{\mathrm{SH},n} \\ 0 & F & F \end{bmatrix} \cdot \begin{bmatrix} \{\alpha^{\mathrm{SH}}\} \\ \{\beta^{m,\mathrm{SH}}\} \\ \{\delta^{d,\mathrm{SH}}\} \end{bmatrix}$$
$$= \sum_d \begin{bmatrix} \mathbf{b}^{(1),n} \\ 0 \\ \mathbf{b}^{(2),n} \end{bmatrix}, \tag{25}$$

where the submatrices $D_{i,j}^{\mathrm{SH},n}$ are equivalent to the submatrices $D_{i,j}^n$ and the submatrices $K_{i,j}^{\mathrm{SH},n}$ are equivalent to the submatrices $K_{i,j}^n$, except that the material properties and the periodic Green's functions are now evaluated at the SH frequency instead of the fundamental frequency. Furthermore, since $(\mathbf{E}^{\mathrm{SH}})_\parallel$ and $(\mathbf{H}^{\mathrm{SH}})_\parallel$ are not continuous through the interfaces, the integrals involved in the evaluation of $K_{i,j}^{\mathrm{SH},n}$ [Eq. (11)] exist by means of the Cauchy principal value [39,59,60]. The indexes m and d denote the summation performed over all the metallic and all the dielectric domains, respectively. Note that this formulation is correct only for periodic structures with nontouching metallic domains. The matrix elements requiring the integration of the periodic Green's function or its gradient are evaluated using a singularity subtraction technique ensuring accurate numerical evaluation [40,45]. The submatrix F corresponds to the symmetric product

$$F_{i,j} = \int_{\partial V_n^\Omega} \mathrm{d}S \mathbf{f}_i^d(\mathbf{r}) \cdot \mathbf{f}(\mathbf{r})_j^d, \tag{26}$$

and the elements of the source vectors $\mathbf{b}$ are given by [31,54]

$$b_i^{(1),d} = \frac{1}{2\varepsilon'} \int_{S_i^\Omega} \mathrm{d}S \nabla_\parallel \cdot \mathbf{f}_i^d(\mathbf{r}) P_\perp(\mathbf{r}), \tag{27}$$

$$b_i^{(2),d} = \frac{1}{\varepsilon'} \sum_l p_l \int_{S_i^\Omega \cap S_l^\Omega} \mathrm{d}S \mathbf{f}_i^d(\mathbf{r}) \cdot (\hat{\mathbf{n}}_d \times \mathbf{f}_l^d(\mathbf{r})), \tag{28}$$

where S_i^Ω is the support of the RWG function $\mathbf{f}_i^d$ in the unit cell and p_l is the expansion coefficient of $\nabla_\parallel P_\perp$ on the RGW function $\mathbf{f}_l^d$ [60]. Finally, the SH electric and magnetic fields scattered by the periodic nanostructure are given by

$$\mathbf{E}_m^{\mathrm{SH}}(\mathbf{r}) = \sum_i -i2\omega\mu_m \int_{\partial V_m^\Omega} \mathrm{d}S' \bar{\mathbf{G}}_m^{\mathrm{SH}}(\mathbf{r}',\mathbf{r}) \cdot \alpha_i^{\mathrm{SH}} \mathbf{f}_i^m(\mathbf{r}')$$
$$- \int_{\partial V_m^\Omega} \mathrm{d}S' [\nabla' \times \bar{\mathbf{G}}_m^{\mathrm{SH}}(\mathbf{r}',\mathbf{r})] \cdot \beta_i^{m,\mathrm{SH}} \mathbf{f}_i^m(\mathbf{r}'), \tag{29}$$

$$\mathbf{H}_m^{\mathrm{SH}}(\mathbf{r}) = \sum_i -i2\omega\varepsilon_m \int_{\partial V_m^\Omega} \mathrm{d}S' \bar{\mathbf{G}}_m^{\mathrm{SH}}(\mathbf{r}',\mathbf{r}) \cdot \beta_i^{m,\mathrm{SH}} \mathbf{f}_i^m(\mathbf{r}')$$
$$+ \int_{\partial V_m^\Omega} \mathrm{d}S' [\nabla' \times \bar{\mathbf{G}}_m^{\mathrm{SH}}(\mathbf{r}',\mathbf{r})] \cdot \alpha_i^{\mathrm{SH}} \mathbf{f}_i^m(\mathbf{r}') \tag{30}$$

in the metallic domains and by

$$\mathbf{E}_d^{\mathrm{SH}}(\mathbf{r}) = \sum_i -i2\omega\mu_d \int_{\partial V_d^\Omega} \mathrm{d}S' \bar{\mathbf{G}}_d^{\mathrm{SH}}(\mathbf{r}',\mathbf{r}) \cdot \alpha_i^{\mathrm{SH}} \mathbf{f}_i^d(\mathbf{r}')$$
$$- \int_{\partial V_d^\Omega} \mathrm{d}S' [\nabla' \times \bar{\mathbf{G}}_d^{\mathrm{SH}}(\mathbf{r}',\mathbf{r})] \cdot \delta_i^{d,\mathrm{SH}} \mathbf{f}_i^d(\mathbf{r}'), \tag{31}$$

$$\mathbf{H}_d^{\mathrm{SH}}(\mathbf{r}) = \sum_i -i2\omega\varepsilon_d \int_{\partial V_d^\Omega} \mathrm{d}S' \bar{\mathbf{G}}_d^{\mathrm{SH}}(\mathbf{r}',\mathbf{r}) \cdot \delta_i^{d,\mathrm{SH}} \mathbf{f}_i^d(\mathbf{r}')$$
$$+ \int_{\partial V_d^\Omega} \mathrm{d}S' [\nabla' \times \bar{\mathbf{G}}_d^{\mathrm{SH}}(\mathbf{r}',\mathbf{r})] \cdot \alpha_i^{\mathrm{SH}} \mathbf{f}_i^d(\mathbf{r}') \tag{32}$$

in the dielectric domains. These four equations allow for the computation of the SH electromagnetic fields at any point in space.

If the discretized object completely fills the unit cell, a mesh which is translation symmetric on opposite edges is required in order to satisfy the continuity of both linear and SH surface currents. Furthermore, the following periodic boundary conditions are imposed on the surface currents [45]

$$\mathbf{J}_n(\mathbf{r} - \mathbf{t}) = e^{i\mathbf{k}\cdot\mathbf{t}} \mathbf{J}_n(\mathbf{r}), \tag{33}$$

$$\mathbf{M}_n(\mathbf{r} - \mathbf{t}) = e^{i\mathbf{k}\cdot\mathbf{t}} \mathbf{M}_n(\mathbf{r}), \tag{34}$$

$$\mathbf{J}_{m,d}^{\mathrm{SH}}(\mathbf{r} - \mathbf{t}) = e^{i\mathbf{K}\cdot\mathbf{t}} \mathbf{J}_{m,d}^{\mathrm{SH}}(\mathbf{r}), \tag{35}$$

$$\mathbf{M}_{m,d}^{\mathrm{SH}}(\mathbf{r} - \mathbf{t}) = e^{i\mathbf{K}\cdot\mathbf{t}} \mathbf{M}_{m,d}^{\mathrm{SH}}(\mathbf{r}). \tag{36}$$

Note again here that the Bloch vector $\mathbf{K} = 2\mathbf{k}$ is associated with the SH waves. If two edges are separated by a lattice vector, the associated expansion coefficients must be identical. The RWG function associated with this edge is defined over the existing border triangle inside the unit cell and translation of the triangle is attached to the opposite discarded edges.

4. NUMERICAL EXAMPLES

In this section, the numerical method described above is assessed using two different experimental configurations. The surface plasmon enhancement of SHG from a gold film is first considered by computing the spectral dependence of the reflected SH intensity. In the second example, the SHG from L-shaped nanoparticle arrays is investigated demonstrating that the computed SH fields fulfill the required symmetry properties imposed by the sample geometry. Note that the presented method focus on the nonlinear response of the metal/dielectric interfaces but the SH signal from noncentrosymmetric media can also be important for the design of nonlinear metamarials [34,61,62].

A. Surface Plasmon Enhancement of the Second-Harmonic Generation from a Gold Film

Let us consider the SH reflected by perfectly flat gold slabs. The slab thickness L varies from 30 to 50 nm. The upper part of the slab is covered with glass and the other interface is a gold/air interface. This sample geometry corresponds to the Kretschmann configuration for excitation of surface plasmon polaritons [63]. The mesh used for the computation in the case of a slab with $L = 50$ nm is shown in Fig. 1(a). Note that the SIE requires only the discretization of the scatterer surface, which is composed of two 100 nm × 100 nm parallel squares filling the unit cell entirely, mimicking an infinite slab between two media [Fig. 1(a)]. The number of degrees of freedom (DOF) is three times the number of edges in the mesh since three unknowns are associated to a given edge (corresponding to the expansion coefficients of the nonlinear surface currents) contrary to the linear problem for which the DOF is twice the number of edges [40,64]. For this problem, the number of DOF per unit area is 4×10^{-2} DOF/nm^2 at the fundamental wavelength and 6×10^{-2} DOF/nm^2 at the SH wavelength ensuring the numerical convergence at both steps. Note that a finer mesh is in general required for an accurate evaluation of the SH problem than for the linear one. The incident wave is a transverse magnetic (TM) plane wave at 45° incidence. The dielectric constants of gold are extrapolated from the experimental data [65]. The tangential component of the fundamental electric field evaluated 1 nm below the glass/gold interface is shown as a function of the incident wavelength in Fig. 1(b). An enhancement of the electric field close to the interface is clearly observed at the plasmon resonances. The influence of the slab thickness on the plasmon resonance wavelength and width is in excellent agreement with T-matrix computations (not shown). Indeed, the surface plasmon resonance redshifts as the slab thickness decreases. Let us now consider the SH reflected by the gold slab. For simplicity, only the component $\chi^{(2)}_{\perp\|\|}$ of the nonlinear polarization is taken into account. Indeed, even if this component is not the largest one for a gold interface [24], surface plasmon resonances lead to a strong enhancement of the tangential component of the fundamental electric field just below the glass/gold interface [Fig. 1(b)]. The purpose of the present part is not to determine the origin of the SHG from such a gold slab but to verify the validity of our formulation [24].

Figure 1(c) shows the reflected SH intensity computed as a function of the incident wavelength. The SH intensity is evaluated in the far-field 50 μm above the gold slab, in the glass medium. Note that the contribution of both glass/gold and
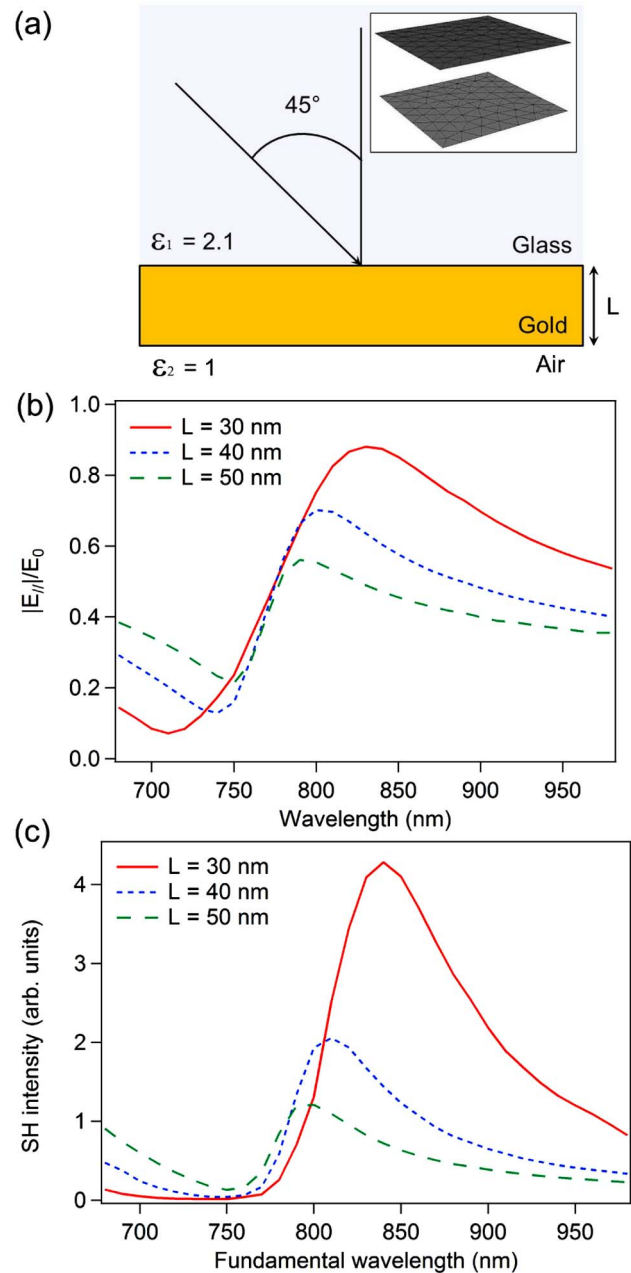
Fig. 1.   (a) Sketch of the geometry used for the computation of the SHG from a gold slab of thickness L. The upper medium is made of glass and the lower medium is air. The incident wave is a TM plane wave at 45° incidence propagating in the glass medium. The mesh used for the computation is shown in the inset. (b) The tangential component of the fundamental electric field evaluated using Eq. (14) 1 nm below the glass/gold interface as a function of the incident wavelength for different slab thicknesses L. The amplitude of the electric field is normalized to the amplitude of the incident electric field. (c) Reflected SH intensity as a function of the fundamental wavelength for the same gold slab, evaluated in the far-field 50 μm above the slab, in the glass medium.

gold/air interfaces are taken into account in the computation of the SH intensity. The spectral dependence of the SH intensity is related to that of the tangential component of the fundamental electric field. Indeed, the SH intensity is proportional to the nonlinear polarization squared, i.e., to $|E_\|^4|$ in the present case, as was also observed experimentally [66–68]. Comparing Figs. 1(b) and 1(c), we observe that this

condition is also fulfilled in our calculation. Computations considering the component $\chi^{(2)}_{\perp\perp\perp}$ of the nonlinear polarization have also been performed (data not shown). An increase of the reflected SH intensity is also observed in that case, since the normal component of the fundamental electric field increases. These results demonstrate that the numerical scheme proposed in this article for the computation of the SHG from periodic structures provides spectral dependences in agreement with the underlying physics. In the following, the polarization dependence of the SHG from nanoparticle arrays is considered.

B. Second-Harmonic Generation from L-Shaped Gold Nanoparticle Arrays

The SHG from periodic arrays of metallic nanoparticles and metamaterials has been widely studied in the past [14–19,22]. In particular, Kauranen *et al.* recently demonstrated that the nonlinear optical response of L-shaped nanoparticle arrays strongly depend on the ordering of the constituting nanoparticles [22]. This dependence is explained by polarization-dependent plasmonic resonances modified by long-range coupling. As an example, they compared the second-order nonlinear optical response of two samples with minor changes in the nanoparticle organizations [Figs. 2(a) and 2(b)]. The two considered arrangements are called sample A and sample B. The nanoparticle's arm length and width are 250 and 100 nm, respectively. The nanoparticle thickness is 20 nm. The period is 500 nm along the u and v directions. Contrary to the experiments reported by Husu *et al.* [22], all the computations presented in this part are performed in vacuum. Let us use the numerical method developed in this paper to compute the SH properties of these two samples. For all the results presented in this section, only the component $\chi^{(2)}_{\perp\perp\perp}$ of the nonlinear surface polarization is considered, since it is the dominant one in the case of SHG from metallic nanoparticles [25]. The fundamental wavelength λ is fixed at 1060 nm. As a consequence, the dispersion of $\chi^{(2)}_{\perp\perp\perp}$ can be neglected in the following and this tensor element is chosen equal to one. The amplitude of the incident wave was also fixed to one and the computed SH intensities are then relative to each other. Figures 2(c) and 2(d) show the SH intensity as a function of the incident polarization for a SH signal polarized along the vector v (squares) and along the vector u (circles). The SH intensity is evaluated at 50 μm from the sample, in the forward direction. As reported by Husu *et al.*, the SH intensity strongly depends on the sample geometry [22]. The u-polarized SH wave is considered first. For both samples, the SH intensity vanishes for u- and v-polarized incident waves and the SH intensity is maximum for intermediate polarization states. This behavior is explained by the mirror symmetry of the nanoparticle organization, which limits the number of nonvanishing tensor elements [69]. Indeed, the macroscopic response of the sample can be described by a nonlinear response tensor A_{jkl} linking the incoming fundamental wave with the outgoing SH wave [69]

$$E_j(2\omega) = \sum_{k,l} A_{jkl} E_k(\omega) E_l(\omega). \qquad (37)$$

Due to the mirror plane in the v-direction, the tensor elements with odd number of index u must vanish [69]. The results
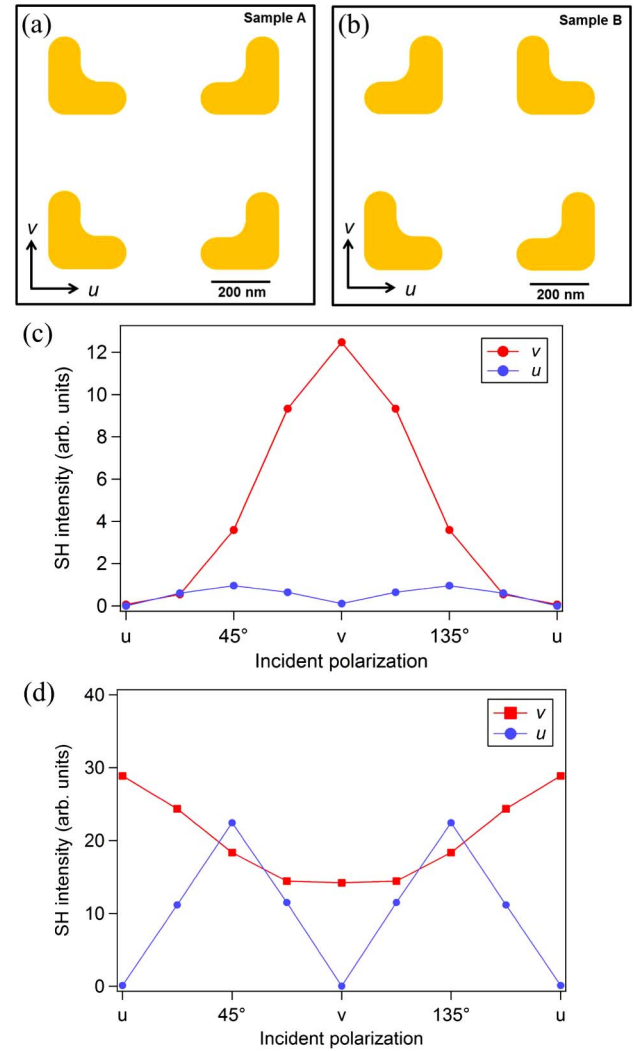
Fig. 2. (a) and (b) Sketch of the nanoparticle array sample A and sample B discussed in the text. The nanoparticle arm length and width are 250 and 100 nm, respectively. The nanoparticle thickness is 20 nm. The unit cell dimension is 1 μm × 1 μm. Computed SH intensities as a function of the incident polarization for (c) sample A and (d) sample B considering the SH signal polarized along the vector v (squares) and along the vector u (circles).

obtained with our method clearly fulfill this selection rule for both sample A and B (Fig. 2).

Now we turn our attention to the v-polarized SH wave. Contrary to the u-polarized SH wave, the polarization of the SH signal depends on the sample geometry. Indeed, the SH intensity from sample A is maximum for a v-polarized incident wave while the SH intensity from sample B is maximum for a u-polarized incident wave. In order to understand the relation between the sample geometry and the SHG, the near-field distributions at both the fundamental and SH wavelengths are shown for sample A (Fig. 3) and sample B (Fig. 4). Figures 3(a)–3(d) and 4(a)–4(d) show the local field intensity at the fundamental wavelength evaluated at the middle of the nanoparticles ($z = 0$ nm) for the u and v components. Considering all the different input/output polarization configurations and comparing the near-field properties at the fundamental wavelength and the far-field SH intensity for each couple of polarization states, it is obvious that the SHG is minimum
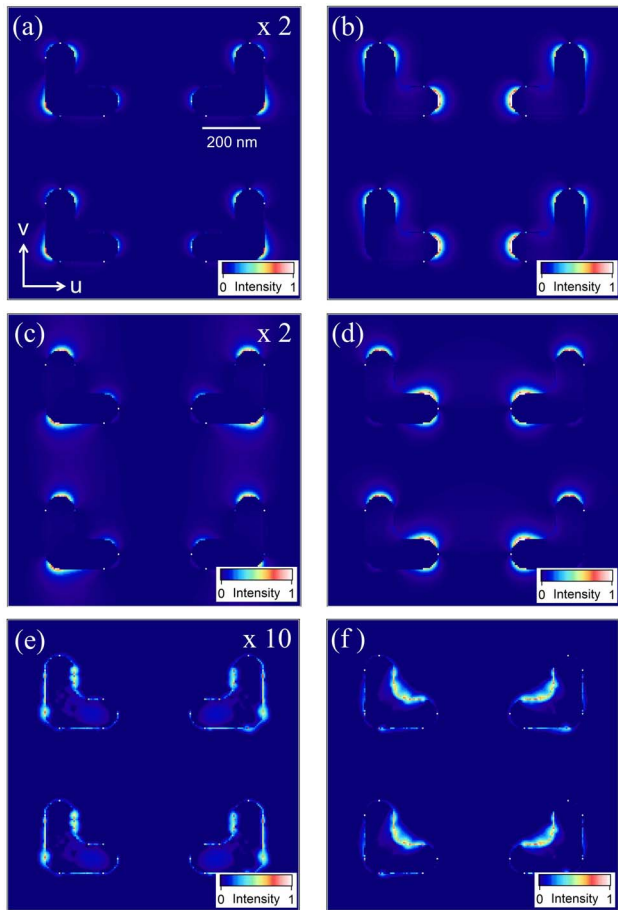
Fig. 3. Near-field distributions of fundamental intensities evaluated for (a) and (b) the *u*-component, and (c) and (d) the *v*-component of the electric field computed for sample A considering (a) and (c) a *u*-polarized, and (b) and (d) a *v*-polarized incident wave. The same color scale is used for all the plots but some have been multiplied by 2 for clarity. Near-field distributions of the SH intensity computed for sample A considering (e) a *u*-polarized and (f) a *v*-polarized incident wave shown in a logarithmic scale. The SH intensity in (e) has been multiplied by 10 for clarity.

Fig. 4. Near-field distributions of fundamental intensities evaluated for (a) and (b) the *u*-component, and (c) and (d) the *v*-component of the electric field computed for sample B considering (a) and (c) a *u*-polarized, and (b) and (d) a *v*-polarized incident wave. For comparison, the color scale is identical to the one in Figs. 3(a)–3(d). Near-field distributions of the SH intensity computed for sample B considering (e) a *u*-polarized and (f) a *v*-polarized incident wave shown in a logarithmic scale.

when the hotspots on a given nanoparticle of the sample are facing hotspots on another nanoparticle, see Figs. 3(a)–3(c) and Figs. 4(a) and 4(b). Indeed, a strong fundamental near-field intensity does not necessarily lead to a high SH signal since SHG is a coherent process and destructive interferences may occur in the far-field region. This phenomenon was reported in the case of SHG from symmetric nanoantennas. Despite an enhancement of the fundamental intensity in nanogap, the corresponding SH intensity is weak due to destructive interferences between out-of-phase nonlinear sources [8]. As previously mentioned, the SH response in gold is dominated by the tensor element $\chi^{(2)}_{\perp\perp\perp}$ and the nonlinear polarization is then perpendicular to nanoparticle surfaces. As a consequence, the contributions of facing electromagnetic hotspots to the scattered SH wave are inclined to cancel out. If destructive interferences are sometimes predicted by the mirror symmetry of the sample [see Figs. 3(a) and 3(b) and Figs. 4(a) and 4(b)], they could also occur in other cases due to specific fundamental near-field distribution, as visible in Fig. 3(c) for the case of the *v*-component of the electric near-field. On the other hand, the far-field SH intensity is

maximum when the hotspots on a given nanoparticle are not facing hotspots on the neighboring nanoparticles, see Figs. 3(d), 4(c), and 4(d). Indeed, destructive interferences are not expected in the latter case. Let us finally note that for experimental measurements, nanodefects in the fabricated structures can produce some discrepancy between experimental results and theoretical predictions [21]. In conclusion, while symmetry selection rules provide insight into the nonlinear optical properties of periodic nanoparticle arrays, these results clearly demonstrate that complete electromagnetic computations are required to fully predict and understand them.

5. CONCLUSIONS

In summary, a surface integral formulation for SHG from periodic metal/dielectric nanostructures has been presented. The linear optical response was first computed at the fundamental wavelength and the nonlinear polarization, i.e., the SH source, and was then evaluated at the metallic interfaces. A surface integral formulation for SHG was then introduced considering the periodicity of the SH electromagnetic wave. In order to ensure accurate results even at resonant conditions, both

the fundamental and SH surface currents were expanded using RWG functions and a PMCHWT formulation was applied. The evaluation of the periodic Green's functions was performed by Ewald's method in order to reduce the overall computation time. The accuracy of the proposed method was assessed using two experimentally-relevant cases. First, the surface plasmon enhancement of SHG from a gold film was considered showing that the computed spectral response is in agreement with phenomenological predictions. As a second example, the SHG from L-shaped nanoparticle array was investigated in detail, demonstrating that the computed SH fields fulfill the required symmetry properties imposed by the sample geometry. The proposed method is versatile and can be used to investigate the second-order nonlinear optical response for nanoparticle arrays [70,71], metallic subwavelength hole arrays [72,73], and metamaterials [74–76]. Furthermore, the proposed numerical scheme paves the way for a deeper investigation of the SHG driven by long-range surface plasmon polaritons and the impact of the mode symmetry [77–79]. The proposed numerical scheme can also be extended to the computation of SHG from plasmonic systems embedded in multilayered systems using suitable Green's functions [80,81].

ACKNOWLEDGMENTS

REFERENCES

1. M. Kauranen and A. V. Zayats, "Nonlinear plasmonics," Nat. Photonics **6**, 737–748 (2012).
2. S. Roke and G. Gonella, "Nonlinear light scattering and spectroscopy of particles and droplets in liquids," Annu. Rev. Phys. Chem. **63**, 353–378 (2012).
3. E. C. Hao, G. C. Schatz, R. C. Johnson, and J. T. Hupp, "Hyper-Rayleigh scattering from silver nanoparticles," J. Chem. Phys. **117**, 5963–5966 (2002).
4. J. Butet, G. Bachelier, I. Russier-Antoine, C. Jonin, E. Benichou, and P.-F. Brevet, "Interferences between selected dipoles and octupoles in the optical second-harmonic generation from spherical gold nanoparticles," Phys. Rev. Lett. **105**, 077401 (2010).
5. J. Butet, J. Duboisset, G. Bachelier, I. Russier-Antoine, E. Benichou, C. Jonin, and P.-F. Brevet, "Optical second harmonic generation of single metallic nanoparticles embedded in a homogeneous medium," Nano Lett. **10**, 1717–1721 (2010).
6. Y. Zhang, N. K. Grady, C. Ayala-Orozco, and N. J. Halas, "Three-dimensional nanostructures as highly efficient generators of second harmonic light," Nano Lett. **11**, 5519–5523 (2011).
7. A. Slablab, L. Le Xuan, M. Zielinski, Y. de Wilde, V. Jacques, D. Chauvat, and J.-F. Roch, "Second-harmonic generation from coupled plasmon modes in a single dimer of gold nanospheres," Opt. Express **20**, 220–227 (2012).
8. J. Berthelot, G. Bachelier, M. Song, P. Rai, G. Colas des Francs, A. Dereux, and A. Bouhelier, "Silencing and enhancement of second-harmonic generation in optical gap antennas," Opt. Express **20**, 10498–10508 (2012).
9. K. Thyagarajan, S. Rivier, A. Lovera, and O. J. F. Martin, "Enhanced second-harmonic generation from double resonant plasmonic antennae," Opt. Express **20**, 12860–12865 (2012).
10. M. W. Klein, C. Enkrich, M. Wegener, and S. Linden, "Second-harmonic generation from magnetic meta-materials," Science **313**, 502–504 (2006).
11. K. Thyagarajan, J. Butet, and O. J. F. Martin, "Augmenting second harmonic generation using Fano resonances in plasmonic systems," Nano Lett. **13**, 1847–1851 (2013).
12. A. Bouhelier, M. Beversluis, A. Hartschuh, and L. Novotny, "Near-field second-harmonic generation induced by local field enhancement," Phys. Rev. Lett. **90**, 013903 (2003).
13. C. C. Neascu, G. A. Reider, and M. B. Raschke, "Second-harmonic generation from nanoscopic metal tips: symmetry selection rules for single asymmetric nanostructures," Phys. Rev. B **71**, 201402 (2005).
14. C. Awada, C. Jonin, F. Kessi, P. M. Adam, S. Kostcheev, R. Bachelot, P. Royer, M. Samah, I. Russier-Antoine, E. Benichou, G. Bachelier, and P.-F. Brevet, "Polarized second harmonic response of square, hexagonal and random arrays of gold metallic nanocylinders," Opt. Mater. **33**, 1440–1444 (2011).
15. B. K. Canfield, S. Kujala, K. Laiho, K. Jefimovs, J. Turunen, and M. Kauranen, "Chirality arising from small defects in gold nanoparticle arrays," Opt. Express **14**, 950–955 (2006).
16. S. Kujala, B. K. Canfield, M. Kauranen, Y. Svirko, and J. Turunen, "Multipolar analysis of second-harmonic radiation from gold nanoparticles," Opt. Express **16**, 17196–17208 (2008).
17. V. K. Valev, X. Zheng, C. G. Biris, A. V. Silhanek, V. Volskiy, B. De Clercq, O. A. Aktsipetrov, M. Ameloot, N. C. Panoiu, G. A. E. Vandenbosch, and V. V. Moshchalkov, "The origin of second harmonic generation hotspots in chiral optical metamaterials," Opt. Mater. Express **1**, 36–45 (2011).
18. V. K. Valev, "Characterization of nanostructured plasmonic surfaces with second harmonic generation," Langmuir **28**, 15454–15471 (2012).
19. A. Capretti, G. F. Walsh, S. Minissale, J. Trevino, C. Forestiere, G. Miano, and L. Dal Negro, "Multipolar second harmonic generation from planar arrays of Au nanoparticles," Opt. Express **20**, 15797–15806 (2012).
20. G. Bautista, M. J. Huttunen, J. Mäkitalo, J. M. Kontio, J. Simonen, and M. Kauranen, "Second-harmonic generation imaging of metal nano-objects with cylindrical vector beams," Nano Lett. **12**, 3207–3212 (2012).
21. J. Butet, K. Thyagarajan, and O. J. F. Martin, "Ultrasensitive optical shape characterization of gold nanoantennas using second harmonic generation," Nano Lett. **13**, 1787–1792 (2013).
22. H. Husu, R. Siikanen, J. Mäkitalo, J. Lehtolahti, J. Laukkanen, M. Kuittinen, and M. Kauranen, "Metamaterials with tailored nonlinear optical response," Nano Lett. **12**, 673–677 (2012).
23. J. Butet, I. Russier-Antoine, C. Jonin, N. Lascoux, E. Benichou, and P.-F. Brevet, "Sensing with multipolar second harmonic generation from spherical metallic nanoparticles," Nano Lett. **12**, 1697–1701 (2012).
24. F. X. Wang, F. J. Rodríguez, W. M. Albers, R. Ahorinta, J. E. Sipe, and M. Kauranen, "Surface and bulk contributions to the second-order nonlinear optical response of a gold film," Phys. Rev. B **80**, 233402 (2009).
25. G. Bachelier, J. Butet, I. Russier-Antoine, C. Jonin, E. Benichou, and P.-F. Brevet, "Origin of optical second-harmonic generation in spherical gold nanoparticles: local surface and nonlocal bulk contributions," Phys. Rev. B **82**, 235403 (2010).
26. J. I. Dadap, J. Shan, and T. F. Heinz, "Theory of optical second-harmonic generation from a sphere of centrosymmetric materials: small-particle limit," J. Opt. Soc. Am. B **21**, 1328–1347 (2004).
27. Y. Pavlyukh and W. Hübner, "Nonlinear Mie scattering from spherical particles," Phys. Rev. B **70**, 245434 (2004).
28. J. Butet, I. Russier-Antoine, C. Jonin, N. Lascoux, E. Benichou, and P.-F. Brevet, "Nonlinear Mie theory for the second harmonic generation in metallic nanoshells," J. Opt. Soc. Am. B **29**, 2213–2221 (2012).
29. A. G. F. de Beer and S. Roke, "Nonlinear Mie theory for second-harmonic generation and sum-frequency scattering," Phys. Rev. B **79**, 155420 (2009).
30. G. Bachelier, I. Russier-Antoine, E. Benichou, C. Jonin, and P.-F. Brevet, "Multipolar second-harmonic generation in noble metal nanoparticles," J. Opt. Soc. Am. B **25**, 955–960 (2008).
31. J. Mäkitalo, S. Suuriniemi, and M. Kauranen, "Boundary element method for surface nonlinear optics of nanoparticles," Opt. Express **19**, 23386–23399 (2011).

32. Y. Zeng, W. Hoyer, J. J. Liu, S. W. Koch, and J. V. Moloney, "Classical theory for second-harmonic generation from metallic nanoparticles," Phys. Rev. B **79**, 235109 (2009).

33. M. Scalora, M. A. Vincenti, D. de Ceglia, V. Roppo, M. Centini, N. Akozbek, and M. J. Bloemer, "Second- and third-harmonic generation in metal-based structures," Phys. Rev. A **82**, 043828 (2010).

34. M. A. Vincenti, D. Ceglia, V. Roppo, and M. Scalora, "Harmonic generation in metallic, GaAs-filled nanocavities in the enhanced transmission regime at visible and UV wavelengths," Opt. Express **19**, 2064–2078 (2011).

35. C. Cirací, E. Poutrina, M. Scalora, and D. R. Smith, "Second-harmonic generation in metallic nanoparticles: clarification of the role of the surface," Phys. Rev. B **86**, 115451 (2012).

36. T. Laroche, F. I. Baida, and D. Van Labeke, "Three-dimensional finite-difference time-domain study of enhanced second-harmonic generation at the end of a apertureless scanning near-field optical microscope metal tip," J. Opt. Soc. Am. B **22**, 1045–1051 (2005).

37. B.-L. Wang, M.-L. Ren, J.-F. Li, and Z.-Y. Li, "Plasmonic coupling effect between two gold nanospheres for efficient second-harmonic generation," J. Appl. Phys. **112**, 083102 (2012).

38. A. Benedetti, M. Centini, M. Bertolotti, and C. Sibilia, "Second harmonic generation from 3D nanoantennas: on the surface and bulk contributions by far-field pattern analysis," Opt. Express **19**, 26752–26767 (2011).

39. C. Forestiere, A. Capretti, and G. Miano, "Surface integral method for second harmonic generation in metal nanoparticles including both local-surface and nonlocal-bulk sources," J. Opt. Soc. Am. B **30**, 2355–2364 (2013).

40. A. M. Kern and O. J. F. Martin, "Surface integral formulation for 3D simulation of plasmonic and high permittivity nanostructures," J. Opt. Soc. Am. A **26**, 732–740 (2009).

41. A. M. Kern and O. J. F. Martin, "Excitation and reemission of molecules near realistic plasmonic nanostructures," Nano Lett. **11**, 482–487 (2011).

42. W. Nakagawa, R.-C. Tyan, and Y. Fainman, "Analysis of enhanced second-harmonic generation in periodic nanostructures using modified rigorous coupled-wave analysis in the undepleted-pump approximation," J. Opt. Soc. Am. A **19**, 1919–1928 (2002).

43. B. Bai and J. Turunen, "Fourier modal method for the analysis of second-harmonic generation in two-dimensionally periodic structures containing anisotropic materials," J. Opt. Soc. Am. B **24**, 1105–1112 (2007).

44. W. L. Schaich, "Second harmonic generation by periodically-structured metal surfaces," Phys. Rev. B **78**, 195416 (2008).

45. B. Gallinet, A. M. Kern, and O. J. F. Martin, "Accurate and versatile modeling of electromagnetic scattering on periodic nanostructures with a surface integral approach," J. Opt. Soc. Am. A **27**, 2261–2271 (2010).

46. B. Gallinet and O. J. F. Martin, "Scattering on plasmonic nanostructures arrays modeled with a surface integral formulation," Photon. Nanostr. Fundam. Appl. **8**, 278–284 (2010).

47. I. Stevanovic, P. Crespo-Valero, K. Blagovic, F. Bongard, and J. R. Mosig, "Integral-equation analysis of 3-D metallic objects arranged in 2-D lattices using the Ewald transformation," IEEE Trans. Microw. Theory Tech. **54**, 3688–3697 (2006).

48. S. Rao, D. Wilton, and A. Glisson, "Electromagnetic scattering by surfaces of arbitrary shape," IEEE Trans. Antennas Propag. **30**, 409–418 (1982).

49. T. K. Wu and L. L. Tsai, "Scattering from arbitrarily-shaped lossy dielectric bodies of revolution," Radio Sci. **12**, 709–718 (1977).

50. R. F. Harrington, *Field Computation by Moment Methods* (Macmillan, 1968).

51. G. R. Cowper, "Gaussian quadrature formulas for triangle," Int. J. Numer. Methods Eng. **7**, 405–408 (1973).

52. I. Hanninen, M. Taskinen, and J. Sarvas, "Singularity subtraction integral formulae for surface integral equations with RWG, rooftop and hybrid basis functions," PIER **63**, 243–278 (2006).

53. J. E. Sipe, V. C. Y. So, M. Fukui, and G. I. Stegeman, "Analysis of second-harmonic generation at metal surfaces," Phys. Rev. B **21**, 4389–4402 (1980).

54. V. Mizrahi and J. E. Sipe, "Phenomenological treatment of surface second-harmonic generation," J. Opt. Soc. Am. B **5**, 660–667 (1988).

55. D. Krause, C. W. Teplin, and C. T. Rogers, "Optical surface second harmonic measurements of isotropic thin-film metals: gold, silver, copper, aluminum, and tantalum," J. Appl. Phys. **96**, 3626–3634 (2004).

56. A. Liebsch, "Second-harmonic generation at simple metal surfaces," Phys. Rev. Lett. **61**, 1233–1236 (1988).

57. M. Corvi and W. L. Schaich, "Hydrodynamic-model calculation of second-harmonic generation at a metal surface," Phys. Rev. B **33**, 3688–3695 (1986).

58. T. F. Heinz, "Second-order nonlinear optical effects at surfaces and interfaces," in *Nonlinear Surface Electromagnetic Phenomena*, H.-E. Ponath and G. I. Stegeman, eds. (Elsevier, 1991).

59. C. Forestiere, G. Iadarola, G. Rubinacci, A. Tamburrino, L. Dal Negro, and G. Miano, "Surface integral formulations for the design of plasmonic nanostructures," J. Opt. Soc. Am. A **29**, 2314–2327 (2012).

60. J. Mäkitalo, S. Suuriniemi, and M. Kauranen, "Boundary element method for surface nonlinear optics of nanoparticles: erratum," Opt. Express **21**, 10205–10206 (2013).

61. W. Fan, S. Zhang, K. J. Malloy, S. R. J. Brueck, N. C. Panoiu, and R. M. Osgood, "Second harmonic generation from patterned GaAs inside a subwavelength metallic hole array," Opt. Express **14**, 9570–9575 (2006).

62. E. H. Barakat, M.-P. Bernal, and F. I. Baida, "Second harmonic generation enhancement by use of annular aperture arrays embedded into silver and filled by lithium niobate," Opt. Express **18**, 6530–6536(2010).

63. J. Homola, *Surface Plasmon Resonance Based Sensors* (Springer, 2006).

64. A. M. Kern and O. J. F. Martin, "Pitfalls in the determination of optical cross sections from surface integral equation simulations," IEEE Trans. Antennas Propag. **58**, 2158–2161 (2010).

65. P. B. Johnson and R. W. Christy, "Optical constants of the noble metals," Phys. Rev. B **6**, 4370–4379 (1972).

66. H. Sonnenberg and H. Heffner, "Experimental study of optical second-harmonic generation in silver," J. Opt. Soc. Am. **58**, 209–211 (1968).

67. H. J. Simon, D. E. Mitchell, and J. G. Watson, "Optical second-harmonic generation with surface plasmons in silver films," Phys. Rev. Lett. **33**, 1531–1534 (1974).

68. R. Naraoka, H. Okawa, K. Hashimoto, and K. Kajikawa, "Surface plasmon resonance enhanced second-harmonic generation in Kretschmann configuration," Opt. Commun. **248**, 249–256 (2005).

69. B. K. Canfield, S. Kujala, K. Jefimovs, Y. Svirko, J. Turunen, and M. Kauranen, "A macroscopic formalism to describe the second-order nonlinear optical response of nanostructures," J. Opt. A **8**, S278–S284 (2006).

70. K. D. Ko, A. Kumar, K. H. Fung, R. Ambekar, G. L. Liu, N. X. Fang, and K. C. Toussaint, Jr., "Nonlinear optical response from arrays of Au bowtie nanoantennas," Nano Lett. **11**, 61–65 (2011).

71. R. Czaplicki, H. Husu, R. Siikanen, J. Mäkitalo, M. Kauranen, J. Laukkanen, J. Lehtolahti, and M. Kuittinen, "Enhancement of second-harmonic generation from metal nanoparticles by passive elements," Phys. Rev. Lett. **110**, 093902 (2013).

72. J. A. H. van Nieuwstadt, M. Sandtke, R. H. Harmsen, F. B. Segerink, J. C. Prangsma, S. Enoch, and L. Kuipers, "Strong modification of the nonlinear optical response of metallic subwavelength hole arrays," Phys. Rev. Lett. **97**, 146102 (2006).

73. T. Xu, X. Jiao, G.-P. Zhang, and S. Blair, "Second-harmonic emission from sub-wavelength apertures: effects of aperture symmetry and lattice arrangement," Opt. Express **15**, 13894–13906 (2007).

74. I. V. Shadrivov, A. A. Zharov, and Y. S. Kivshar, "Second-harmonic generation in nonlinear left-handed metamaterials," J. Opt. Soc. Am. B **23**, 529–534 (2006).

75. A. Rose, D. Huang, and D. R. Smith, "Nonlinear interference and unidirectional wave mixing in metamaterials," Phys. Rev. Lett. **110**, 063901 (2013).

76. V. K. Valev, J. J. Baumberg, C. Sibilia, and T. Verbiest, "Chirality and chiroptical effects in plasmonic nanostructures: fundamentals, progress, and outlook," Adv. Mater. **25**, 2517–2534 (2013).

77. J. J. Burke, G. I. Stegeman, and T. Tamir, "Surface-polariton-like waves guided by thin, lossy metal films," Phys. Rev. B **33**, 5186–5201 (1986).

78. P. Berini, "Long-range surface plasmon polaritons," Adv. Opt. Photon. **1**, 484–588 (2009).

79. A. Farhang and O. J. F. Martin, "Plasmon delocalization onset in finite sized nanostructures," Opt. Express **19**, 11387–11396 (2011).

80. Y. P. Chen, W. E. I. Sha, W. C. H. Choy, L. Jiang, and W. C. Chew, "Study on spontaneous emission in complex multilayered plasmonic system via surface integral equation approach with layered medium Green's function," Opt. Express **20**, 20210–20221 (2012).

81. Y. P. Chen, W. C. Chew, and L. Jiang, "A new Green's function formulation for modeling homogeneous objects in layered medium," IEEE Trans. Antennas Propag. **60**, 4766–4776 (2012).